[21] F. Akleman and L. Sevgi, "A novel MoM- and SSPE-based ground-wave-propagation field-strength prediction simulator," *IEEE Antennas Propag. Mag.*, vol. 49, no. 5, pp. 69–82, Oct. 2007.

[22] *ITU-R Rec. P.368-8 Ground-Wave Propagation Curves for Frequencies Between 10 kHz and 30 MHz* International Telecommunication Union, 2005.

[23] G. Prieto, M. M. Vélez, P. Angueira, D. Guerra, D. d. l. Vega, and A. Arrinda, "Digital Radio Mondiale (DRM). field trials for minimum C/N requirements," in *Proc. IBC05*, Sep. 2005, pp. 43–48.

[24] *Document 6E/175-E. Digital Radio Mondiale DRM Daytime MW Tests* International Telecommunication Union, 2005.

[25] *Digital Radio Mondiale (DRM): MW Simulcast Tests in México D.F* International Telecommunication Union ITU-R, Document 6E/403-E, 2005.

[26] *DRM Daytime MW Tests for Frequencies Below 1 MHz* International Telecommunication Union ITU-R, Document 6/353-E, 2007.

[27] L. Sevgi, C. Uluisik, and F. Akleman, "A Matlab-based two-dimensional parabolic equation radiowave propagation package," *IEEE Antennas Propag. Mag.*, vol. 47, no. 4, pp. 184–195, Aug. 2005.

[28] D. de la Vega, S. López, D. Guerra, G. Prieto, M. M. Vélez, and P. Angueira, "Analysis of the attenuation caused by the influence of orography in the medium wave band," in *IEEE 65th Vehicular Tech. Conf.*, Dublin, Ireland, Apr. 2007.

[29] *World Atlas of Ground Conductivities* International Telecommunication Union ITU-R Recommendation P.832-2, 1999.

[30] *Monitoring of the Radio Coverage of Land Mobile Networks to Verify Compliance with a Given License* International Telecommunication Union ITU-R, Recommendation SM.1447, 2000.

# A Frequency-Dependence Model for the Ultrawideband Channel Based on Propagation Events

Camillo Gentile and Alfred Kik

*Abstract*—While the frequency dependence of the wireless channel may be negligible for narrow to wideband signals, it has been shown that modeling this dependence for bandwidths in excess of 2 GHz improves channel reconstruction up to 40%. Yet to our knowledge, only Molisch *et al.* have done so for the ultrawideband channel. Their benchmark frequency model however represents the average dependence over the collection of multipath arrivals in the channel rather than that of individual arrivals. Building on the geometric theory of diffraction, we propose a novel stochastic frequency model for *individual* arrivals according to the propagation events on their paths between the transmitter and receiver. We extract the model parameters from an extensive measurement campaign of 4000 channel frequency sweeps in four separate buildings combined with raytracing simulations, and show that ours fits the gathered data more closely than the benchmark model.

*Index Terms*—Geometric theory of diffraction (GTD).

## I. INTRODUCTION

Ultrawideband (UWB) signals are characterized by a bandwidth greater than 500 MHz or one exceeding 20% of the center frequency of radiation [1], [2]. The approval of the FCC unlicensed band from 3.1–10.6 GHz in 2002 has prompted a concerted effort in the extensive

modeling of the indoor UWB channel in recent years. Irahhauten [3] provides a comprehensive overview of indoor UWB measurements in the time and frequency domains [4]–[11]. Most references provide channel models characterized by path loss, small-scale fading, and delay spread.

While the frequency dependence of the wireless channel may be negligible for narrow to wideband signals, it has been shown that modeling this dependence for bandwidths in excess of 2 GHz improves channel reconstruction up to 40% [12]. Yet to our knowledge, only Molisch *et al.* have done so for the ultrawideband channel. Their benchmark frequency model however represents the average dependence over the collection of multipath arrivals in the channel rather than that of individual arrivals. This paper proposes a novel stochastic frequency model for *individual* arrivals.

The paper reads as follows: similar to [8]–[11], Section II outlines our channel measurement campaign consisting of a total of 4000 frequency sweeps from 2–6.5 GHz in four separate buildings. The geometric theory of diffraction (GTD) provides a basis for the frequency dependence of individual arrivals according to the propagation events on their paths between the transmitter and receiver. Building on this theory, the first contribution of this paper is the GTD-based frequency model in Section III whose parameters are characterized from the measurement campaign. While significantly more accurate than the benchmark model, it accounts only for the geometry of the buildings and not the material properties of the walls. Section IV describes our main contribution as an extension of the GTD-based model incorporating the material properties as well. The proposed model fits the gathered data more closely than both the benchmark and the GTD-based models as highlighted in the results Section V, following by our conclusions.

## II. PRELIMINARIES

### A. The Frequency-Dependent Indoor Channel

The frequency-dependent indoor channel consists of an impulse train representing $K$ multipath arrivals indexed through $k$ [12]

$$H(f) = \sum_{k=1}^{K} a_k \left( \frac{f}{f_0} \right)^{-\alpha_k} e^{-j2\pi f \tau_k} \quad (1)$$

where $\tau_k$ denotes the delay of the arrival in propagating between the transmitter and receiver and $a_k$ denotes the complex-valued amplitude which accounts for both attenuation and phase shift due to transmission, reflection, and diffraction introduced by walls (and other objects) on its path. The *frequency parameter* $\alpha_k$ quantifies the frequency dependence of the amplitude across the bandwidth of the signal, where $f_0$ is the lower frequency. The frequency-dependent indoor channel has been shown to improve reconstruction up to 40% for bandwidths in excess of 2 GHz [12] relative to the conventional which assumes $\alpha_k = 0$ [13].

### B. The Measurement System

We measured the frequency response of the channel $H(f)$ in the bandwidth $f = 2 - 6.5 \text{ GHz}$ with sampling interval $\Delta f$. The discrete frequency spectrum translates to a signal with period $1/\Delta f$ in the time domain [14]. Choosing $\Delta f = 1.25 \text{ MHz}$ allows for a maximum multipath spread of 800 ns which proves sufficient throughout all four buildings for the arrivals to subside and avoid time aliasing.

Fig. 1 displays the block diagram of our measurement system complete with component specifications. The vector network analyzer emits a series of tones with frequency $f$ at Port 1 and measures the relative amplitude and phase $S_{21}(f)$ at Port 2, providing automatic phase synchronization between the two ports. The synchronization
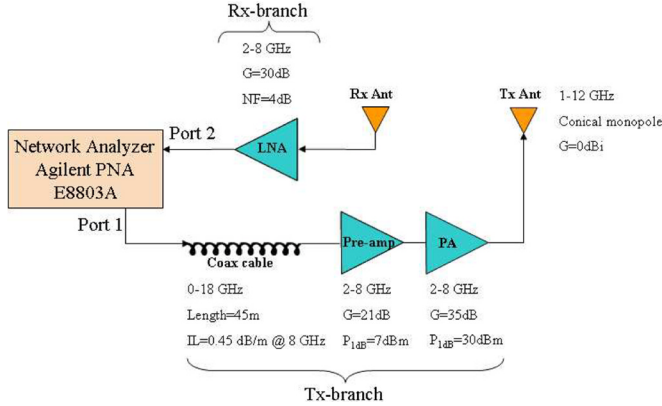
Fig. 1. Block diagram of the measurement system using a vector network analyzer.

TABLE I
EXPERIMENTS CONDUCTED IN MEASUREMENT CAMPAIGN

| building | wall material | LOS range (10) | NLOS range (30) |
|---|---|---|---|
| *NIST* *North* | sheet rock / aluminum studs | 1.2–24.3 m | 1.7–30.5 m max wall#: 9 |
| *Child* *Care* | plaster / wooden studs | 2.0–15.7 m | 4.7–26.7 m max wall#: 6 |
| *Sound* | cinder block | 3.4–45.0 m | 5.9–28.9 m max wall#: 6 |
| *Plant* | steel | 2.9–43.7m | 4.9–32.3m max wall#: 6 |

TABLE II
THE GTD-BASED COMPONENTS OF THE FREQUENCY PARAMETER

| propagation mechanism | $\alpha^P$ |
|---|---|
| free space | 0.0 |
| transmission | 0.0 |
| reflection | 0.0 |
| edge diffraction | 0.5 |
| corner diffration | 1.0 |
| cylinder face diffraction | -0.5 |
| cylinder broadside diffraction | -1.0 |

translates to a common time reference for the transmitted and received signals. The long cable enables variable positioning of the conical monopole antennas from each other throughout the test area. Their height was set to 1.7 m (average human height). The preamplifier and power amplifier on the transmit branch boost the signal such that it radiates at approximately 30 dBm from the antenna. After it passes through the channel, the low-noise amplifier on the receiver branch boosts the signal above the noise floor of Port 2 before feeding it back. The dynamic range of the system corresponds to 140 dB as computed in [9] for an IF bandwidth of 1 kHz and a SNR of 15 dB at the receiver.

The $S_{21}(f)$-parameter of the network can be expressed as a product of the $Tx$-branch, the $Tx$-antenna, the propagation channel, the $Rx$-antenna, and the $Rx$-branch

$$S_{21}(f) = H_{Tx}^{\mathrm{bra}}(f) \cdot H_{Tx}^{\mathrm{ant}}(f) \cdot H(f) \cdot H_{Rx}^{\mathrm{ant}}(f) \cdot H_{Rx}^{\mathrm{bra}}(f)$$
$$= H_{Tx}^{\mathrm{bra}}(f) \cdot \underbrace{H_{Tx}^{\mathrm{ant}}(f) \cdot H_{Rx}^{\mathrm{ant}}(f)}_{H^{\mathrm{ant}}(f)} \cdot H(f) \cdot H_{Rx}^{\mathrm{bra}}(f). \quad (2)$$

The frequency response of the channel $H$ is isolated by individually measuring the transmission responses $H_{Tx}^{\mathrm{bra}}$, $H_{Rx}^{\mathrm{bra}}$, and $H^{\mathrm{ant}}$ in advance and de-embedding them from (2).

To account for the small-scale effects in the measurements, for each experiment we centered a $5 \times 5$ grid constructed from a wooden plank on the floor about the nominal location of the receiver antenna. The distance between the grid points was 15 cm, corresponding to a full wavelength at 2 GHz, ensuring spatial independence between the measured points for a total of 25 sub-experiments.

*C. The Measurement Campaign*

The measurement campaign was conducted in four separate buildings on the NIST campus in Gaitherburg, Maryland, each constructed from a dominant wall material varying from sheet rock to cinder block. Table I summarizes the 40 experiments in each building [10 line-of-sight (LOS) and 30 non line-of-sight (NLOS)], including the maximum number of walls separating the transmitter and receiver.

Spectral estimation methods [15]–[17] exist to decompose the measured frequency response of a sub-experiment into $K$ arrivals parameterized as $(a_k, \alpha_k, \tau_k)$ according to (1). The chosen method becomes increasingly important with the presence of noise in the channel. The *SVD-Prony* [16] and *SVD-Eigenpencil* [17] are two candidate methods robust to high levels of noise. We compared the two in estimating the frequency parameter of the first arrival known as $\alpha_1 = 0$ for free space propagation in the combined 40 LOS experiments from the four buildings. Qiu [17] claims that the *SVD-Eigenpencil* decomposition method

works reliably above an SNR of 15 dB which corresponds to 140 dB path loss for our measurement system (see Section II-B). Hence we filtered out the least significant arrivals with power below the equivalent level of $10^{-7}$ in linear scale. The averages and standard deviations over the $25 \times 40$ sub-experiments yielded $\mu_{\alpha_1} = 0.0912$ and $\sigma_{\alpha_1} = 0.1321$ for the *SVD-Prony* method and $\mu_{\alpha_1} = 0.0387$ and $\sigma_{\alpha_1} = 0.0662$ for the *SVD-Eigenpencil* method, hence we implemented the latter better suited to our application.

### III. THE GTD-BASED FREQUENCY MODEL

The GTD has been invoked in channel characterization [12], [17] to interpret the frequency dependence of an individual arrival according to the sequence of propagation events on its path between the transmitter and receiver. The theory states that each event of the propagation mechanisms classified in Table II contributes a component $\alpha^P$ to the aggregate frequency parameter $\alpha$ of the arrival [18]. The four buildings in the measurement campaign are void for the most part of cylindrical objects such as rounded columns or furniture with dimensions comparable to the signal wavelength[1], allowing us to disregard cylindrical face and broadside diffractions as confirmed through the measurement campaign in which we recorded no arrivals with negative frequency parameter. Corner diffractions can be disregarded as well since the cumulative surface area of corners with respect to edges is negligible in modeling the significant features of the environment.

Henceforth we shall consider only the significant components $(\alpha^T, \alpha^R, \alpha^D)$ of **T**ransmission, **R**eflection, and edge **D**iffraction. The

[1]The lowest frequency in the bandwidth translates to a wavelength of 15 cm.

TABLE III
PARAMETER AND ERROR VALUES OF THE THREE FREQUENCY MODELS

| building | GTD-based model | | Proposed model | | | | Benchmark model | | |
|---|---|---|---|---|---|---|---|---|---|
| | $\lambda^D(\frac{1}{ns})$ | $e(\frac{1}{ps})$ | $\lambda^T(\frac{1}{ns}), \alpha^T$ | $\lambda^R(\frac{1}{ns}), \alpha^R$ | $\lambda^D(\frac{1}{ns}), \alpha^D$ | $e(\frac{1}{ps})$ | $\alpha^{LOS}$ | $\alpha^{NLOS}$ | $e(\frac{1}{ps})$ |
| NIST North | 0.037 | 1.400 | 0.028, 0.124 | 0.042, 0.092 | 0.013, 0.694 | 0.279 | 0.052 | 1.191 | 3.181 |
| Child Care | 0.043 | 1.924 | 0.033, 0.215 | 0.054, 0.069 | 0.017, 0.536 | 0.645 | 0.094 | 1.965 | 4.306 |
| Sound | 0.031 | 7.039 | 0.015, 0.621 | 0.038, 0.051 | 0.013, 0.424 | 2.324 | 0.022 | 3.644 | 17.871 |
| Plant | 0.013 | 0.893 | 0.000, N/A | 0.217, 0.012 | 0.009, 0.452 | 0.723 | 0.013 | 0.078 | 2.430 |

GTD-based model then reduces the frequency parameter of an arrival to the sum of the components of each event on its path or

$$\alpha = \alpha^T \cdot l + \alpha^R \cdot m + \alpha^D \cdot n \qquad (3)$$

where the arrival *order* $(l, m, n)$ represents the number of transmissions, reflections, and diffractions respectively. So as to complete the model for $\alpha$, we formulate a stochastic process for $(l, m, n)$ in the remainder of this section.

Consider an arrival which undergoes a series of propagation events on its path: once an event occurs with delay $\tau$, the delay of the next event $\tau + \Delta\tau$ depends only on the randomly-located objects throughout the environment rather than on $\tau$, meaning that the *interevent delays* $\Delta\tau$ are independent of each other. The Poisson process [19] models this behavior which is governed through the probability density function for $\Delta\tau$

$$f(\Delta\tau|\lambda) = \lambda e^{-\lambda\Delta\tau} \qquad (4)$$

where $1/\lambda$ represents the average delay between events.

Now the probability that a total of $l + m + n$ events have occured on a path arriving with delay $\tau$ follows from (4) as

$$p(l+m+n|\tau, \lambda) = \frac{e^{-\lambda\tau}(\lambda\tau)^{l+m+n}}{(l+m+n)!}. \qquad (5)$$

Further given that $l + m + n$ events have occurred, $(l, m, n)$ are Binomial random variables with respective probabilities $p^T + p^R + p^D = 1$ [19], so

$$p(l, m, n|l+m+n) = \frac{(l+m+n)!}{l!\, m!\, n!}(p^T)^l (p^R)^m (p^D)^n. \qquad (6)$$

Finally the sought probability $p(l, m, n|\tau, \lambda)$ of exactly $l$ transmissions, $m$ reflections, and $n$ diffractions on a path with delay $\tau$ is determined by substituting (5) and (6) into

$$\begin{aligned} &p(l, m, n|\tau, \lambda) \\ &= p(l, m, n|l+m+n) \cdot p(l+m+n|\tau, \lambda) \\ &= \underbrace{\frac{e^{-\lambda^T\tau}(\lambda^T\tau)^l}{l!}}_{p(l|\tau, \lambda^T)} \cdot \underbrace{\frac{e^{-\lambda^R\tau}(\lambda^R\tau)^m}{m!}}_{p(m|\tau, \lambda^R)} \cdot \underbrace{\frac{e^{-\lambda^D\tau}(\lambda^D\tau)^n}{n!}}_{p(n|\tau, \lambda^D)} \end{aligned} \qquad (7)$$

and rearranging such that $\lambda^T = p^T\lambda$, $\lambda^R = p^R\lambda$, and $\lambda^D = p^D\lambda$. This means that provided the parameters $(\lambda^T, \lambda^R, \lambda^D)$, the reconstructed arrival order is drawn from independent Poisson random variables

$$\begin{aligned} l' &\sim \mathcal{P}\left(\mu_{l'} = \lambda^T\tau, \sigma_{l'} = \sqrt{\lambda^T\tau}\right) \\ m' &\sim \mathcal{P}\left(\mu_{m'} = \lambda^R\tau, \sigma_{m'} = \sqrt{\lambda^R\tau}\right) \\ n' &\sim \mathcal{P}\left(\mu_{n'} = \lambda^D\tau, \sigma_{n'} = \sqrt{\lambda^D\tau}\right). \end{aligned} \qquad (8)$$

### A. Extracting the $\lambda^d$-Parameter

Since edge diffraction defaults as the only significant propagation mechanism with nonzero component $\alpha^P$, transmissions and reflections have no effect on $\alpha$. So from (3), the number of diffractions on the path of an arrival directly maps to its frequency parameter as

$$\alpha = 0.5 \cdot n. \qquad (9)$$

As a result, the $\lambda^D$-parameter alone completely specifies the model.

In order to estimate $\lambda^D$, the arrivals from each sub-experiment in Section II-C were grouped together for each building into a measured $(M)$ sample set of $K_M$ total arrivals parameterized as $(a_k, \alpha_k, \tau_k)$. Given the delay $\tau_k$ and the observed diffraction order $n_k = \alpha_k/0.5$ from (9) in the sample set, the Maximum Likelihood Estimation (MLE) [20] yields

$$\lambda^D = \frac{\sum_{k=1}^{K_M} n_k}{\sum_{k=1}^{K_M} \tau_k}. \qquad (10)$$

With $\lambda_D$ known, the reconstructed order is a Poisson random variable $n'$ furnished through (8); the reconstructed frequency parameter follows as $\alpha' = 0.5 \cdot n'$. Observing the sample set, we noticed that the frequency parameter on average increases with arrival delay, a phenomenon consistent with our model. This means that a path with a longer delay will on average have undergone more diffractions on the propagation path.

The weighted mean-squared error

$$e = \frac{1}{K_M}\sum_{k=1}^{K_M} \frac{(\alpha_k - \alpha'_k)^2}{\tau_k} \qquad (11)$$

gauges the fit between the GTD-based model and the sample set. The weight $w_k = 1/\tau_k$ is proportional to the inverse of the variance $\sigma^2_{\alpha'_k} = \left(0.5 \cdot \sigma_{n'_k}\right)^2 = \left(0.5 \cdot \sqrt{\lambda^D\tau_k}\right)^2$ typically used to leverage more reliable points. The values for the $\lambda^D$-parameter of the GTD-based model and the associated error $e$ for the four buildings appear in Table III.

## IV. THE PROPOSED FREQUENCY MODEL

The GTD was developed to characterize the salient features of metal objects such as corners, edges, and curves from radar scattering [18]. The underlying assumption of infinite conductivity renders the frequency parameter dependent only on the object geometry. The theory breaks down for materials with finite conductivity for which material properties and incident angle of diffraction also influence $\alpha$ [21], compromising the values for $\alpha^P$ in Table II and so potentially weighing in the dependences of the other two dominant propagation mechanisms of transmission and reflection.
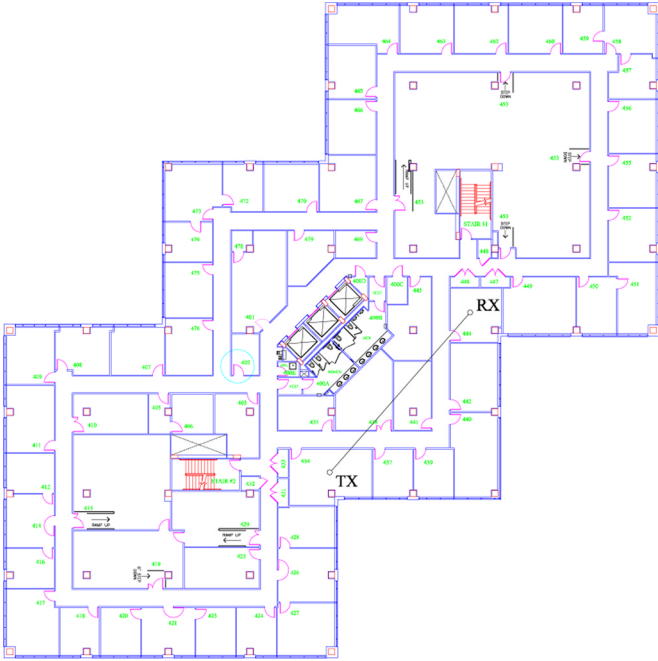
Fig. 2. CAD model of the *NIST North* building.

In this section, we extend the GTD-based model to account for both geometry *and* material properties as *average* effects over the incident angles of the propagation mechanisms. To this end, the proposed model relaxes the prescribed values of $(\alpha^T, \alpha^R, \alpha^D)$ to allow generic $\alpha$-parameters in (3) instead. The values for the $\alpha$-parameters of the proposed model are found empirically in the sequel through the measurement campaign combined with raytracing.

### A. Extracting the $\lambda$-Parameters

In the GTD-based model only the diffraction mechanism is frequency dependent. It follows that the diffraction order $n_k$ of an arrival $k$ can be observed directly from $\alpha_k$, making it easy to calculate $\lambda^D$ through (10). Conversely, the order $(l_k, m_k, n_k)$ in the proposed model cannot be observed from $\alpha_k$, especially when lacking values for the $\alpha$-parameters. Rather we resort to the *Wireless System Engineering Tool (WiSE)* [22], [23] to estimate the $\lambda$-parameters in (7) by simulating the sub-experiments in Section II-C through radio-frequency raytracing. A computer-aided design (CAD) of the building characterizes the propagation environment while the positioning of the transmitter-receiver pair in the building differentiates each sub-experiment[2] (see Fig. 2). In principle three-dimensional raytracing can produce accurate results provided a detailed CAD model coupled with exact building material properties across all frequencies in the investigated band, but in practice simplifications through visibility graphs or rayshooting are necessary to achieve computational feasibility [24], [25]. Moreover, to our knowledge there exists scarce literature on measured building properties across the ultrawideband [26]–[29].

Despite its limitations, German *et al.* have shown *WiSE* to be in excellent agreement with empirical measurements, at least in terms of the arrival times and angular spread, the former of interest to us [30]. This is because the interevent delays and in turn the $\lambda$-parameters depend only on the geometry of the environment and not on the material properties or operation frequency. The operation frequency does however change the dielectric properties of the walls in attenuating the

[2]The CAD models lack office furniture present during the measurement campaign.

amplitude of the arrivals with each propagation event, and as a result affects the number of arrivals delivered when specifying the receiver threshold power. Since the raytracing tool only runs at a single frequency as opposed to wideband operation, we set the raytracing simulations at the center frequency 4.25 GHz of the bandwidth for which the dielectric properties of the walls are available in [26]. We also set the power threshold equal to $10^{-7}$ as in the measurement campaign. Other relevant settings are the transmission power of 30 dBm and the omni-directional emission pattern of the antennas as in Section II-B.

The raytracing tool directly generates the impulse response of a sub-experiment described by a train of $K$ arrivals with complex amplitude and delay $(a_k, \tau_k)$. Of course knowing the propagation mechanisms on the path, the *WiSE* raytracing software has an option to furnish the order of the arrival $(l_k, m_k, n_k)$. Parallel to Section III-A, a simulated (S) sample set of $K_S$ arrivals is gathered from all the sub-experiments in a building from which the MLE for the $\lambda$-parameters yields

$$(\lambda^T, \lambda^R, \lambda^D) = \frac{\sum_{k=1}^{K_S} (l_k, m_k, n_k)}{\sum_{k=1}^{K_S} \tau_k}. \tag{12}$$

### B. Extracting the $\alpha$-Parameters

The $\lambda$-parameters found above leverage the occurrences of the three propagation mechanisms in (3). Now the same measured sample set of $K_M$ arrivals parameterized as $(a_k, \alpha_k, \tau_k)$ used to estimate the $\lambda^D$-parameter of the GTD-based model in Section III-A is used here to estimate rather the $\alpha$-parameters of the proposed model. The delay $\tau_k$ of arrival $k$ maps to the expected reconstructed order $\left(\mu_{l'_k}, \mu_{m'_k}, \mu_{n'_k}\right)$ through the $\lambda$-parameters in (7); the expected reconstructed frequency parameter $\alpha'_k = \alpha^T \cdot \mu_{l'_k} + \alpha^R \cdot \mu_{m'_k} + \alpha^D \cdot \mu_{n'_k}$ follows from (3). The values $(\alpha^T, \alpha^R, \alpha^D)$ can be found by minimizing the weighted mean-squared error (see (11)) between the proposed model and the sample set

$$\min_{\alpha^T, \alpha^R, \alpha^D} e = \frac{1}{K_M} \sum_{k=1}^{K_M} \frac{(\alpha_k - \alpha'_k)^2}{\tau_k}. \tag{13}$$

The values for the $\lambda$-parameters and the $\alpha$-parameters of the proposed model and the associated error $e$ for the four buildings appear in Table III.

## V. RESULTS

### A. The Benchmark Frequency Model

This section compares the proposed model to the GTD-based model, and also to the benchmark model in [11]. In the latter, the frequency parameter represents the average dependence over the collection of arrivals rather than that of individual arrivals, making $\alpha_k = \alpha$ path-independent. Accordingly the $\alpha$-parameter is extracted from the measured sample set in Section III-A using the technique described in [11]. The technique reduces to curve fitting the $\alpha$-parameter to the amplitude of the measured frequency responses. The weighted mean-squared error for the benchmark model is

$$e = \frac{1}{K_M} \sum_{k=1}^{K_M} \frac{(\alpha_k - \alpha)^2}{\tau_k} \tag{14}$$

and the values for the $\alpha$-parameter and the associated error $e$ for the four buildings appear in Table III.

The benchmark model discriminates between LOS and NLOS conditions in computing separate $\alpha^{LOS}$ and $\alpha^{NLOS}$ for each of the four buildings. In LOS conditions, the signal strength of the first arrival is

generally much stronger than the subsequent in the multipath profile, and so its corresponding frequency parameter $\alpha_1 = 0$ contributes significantly more than the others to $\alpha$, hence biasing $\alpha^{LOS}$ closer to 0 compared to $\alpha^{NLOS}$. Rather the path-dependent GTD-based and proposed models can discriminate between the two conditions precisely by explicitly setting the respective probabilities to

$$p(n = 0|\tau_k, \lambda^D)$$
$$= \{\, 1, \quad \text{LOS}, k = 1$$
$$p(l = 0, m = 0, n = 0|\tau_k, \lambda^T, \lambda^R, \lambda^D)$$
$$= \begin{cases} 1, & \text{LOS}, k = 1 \\ 0, & \text{LOS}, k > 1. \\ 0, & \text{NLOS}. \end{cases} \qquad (15)$$

### B. Comparing the Three Models

The benchmark model does not account for the average increase in the frequency parameter with delay observed in the measured sample set in Section III-A. In consequence, the model parameter $\alpha$ tends to be higher than the sample value for paths arriving earlier in the profile and lower for paths arriving later. This justifies the poorest fit of the three models as quantified through the error values $e$ in Table III. While the GTD-based model does account for the average increase in the frequency parameter and in turn delivers a smaller error than the benchmark, it still assumes frequency dependence solely on the diffraction mechanism whose component value $\alpha^D = 0.5$ proves valid only for materials with infinite conductivity. Indeed, amongst the four buildings it yields the least error in *Plant* with steel walls.

The proposed model relaxes the GTD-based assumption by incorporating parameters to characterize lossy materials as well, offering the greatest flexibility to fit the sample set with the smallest error. Even so, the proposed model in comparison witnesses only a mild improvement in *Plant*. The raytracing software returns $\lambda^T = 0$ in this building, indicating no wall transmissions through metal; in contrast, the relatively large value of $\lambda^R$ with respect to the other buildings mirrors the high reflection coefficient of steel which maintains the arrivals above the power threshold in Section IV-A longer, delivering many closely-packed arrivals at the receiver. In fact, even though the paths cannot penetrate walls, the combined signal strength of the arrivals measures greatest in the *Plant* building due to the amount of power reflected back to the receiver.

The characterization of building materials across the UWB spectrum compiled to date provides some insight on the $\alpha$-parameters extracted in the proposed model. Sagnard measured the complex permittivity of eight typical wall materials for frequencies in the band 8–12 GHz [27], including plaster and concrete with properties similar to the wall materials in *Child Care* and *Sound* respectively. The study reports a small negative frequency dependence of the permittivity for all materials. Muqaibel found concurrent results in his analysis of ten wall materials[3] up to 15 GHz [28], including sheet rock and cinder block. Since the reflection coefficient of a material increases with the magnitude of its permittivity [31], the studies suggest a weaker reflected signal at higher frequencies, a phenomenon consistent with the small (relative to $\alpha^T$ and $\alpha^D$) positive values of $\alpha^R$ throughout all four buildings.

The penetration loss of a material quantifies the reduction in power when transmitting through the specimen with respect to free space [26]. The transmission parameter $\alpha^T$ gauges the frequency dependence of the penetration loss, analogous to the slope of the penetration loss versus frequency. Zhang reports a slope of roughly 1.5 dB/GHz for plaster and 2.5 dB/GHz for concrete up to 10 GHz [29], while Muqaibel reports much smaller values of 0.02 dB/GHz

---

[3]Except for brick which showed a small positive slope.

for sheet rock and 0 dB/GHz for cinder block. Keep in mind that the specimens varied both in composition and thickness, as did the testing procedures. As Zhang, we found significant frequency dependences of $\alpha^T$ in sheet rock, plaster, and cinder block as did we notice a much stronger dependence in cinder block (composed from concrete and cinders) relative to plaster.

## VI. Conclusion

Building on the GTD, this paper develops a novel model for the frequency dependence of individual multipath arrivals in a channel based on the number of transmissions, reflections, and diffractions on their paths between the transmitter and receiver. In order to extract the parameters of the model, we conducted a channel measurement campaign composed of 4000 frequency sweeps from 2–6.5 GHz in four separate buildings coupled with raytracing simulations. The proposed model fits the gathered data more closely than existing models, moreover its parameters characterizing the frequency dependence of the building materials are consistent with values previously recorded for the complex permittivity and penetration loss of those materials.

## References

[1] A. F. Molisch, "Ultrawideband propagation channels-theory, measurement, and modeling," *IEEE Trans. Veh. Technol.*, vol. 54, no. 5, pp. 1528–1545, Sep. 2005.

[2] D. Cassioli, M. Z. Win, and A. F. Molisch, "The ultra-wide bandwidth indoor channel: From statistical model to simulations," *IEEE J. Sel. Areas Commun.*, vol. 20, no. 6, pp. 1247–1257, Aug. 2002.

[3] Z. Irahhauten, H. Nikookar, and G. J. M. Janssen, "An overview of ultra wide band indoor channel measurements and modeling," *Proc. IEEE Microw. Wireless Compon. Lett.*, vol. 14, no. 8, pp. 386–388, Aug. 2004.

[4] S. M. Yano, "Investigating the ultra-wideband indoor wireless channel," in *Proc. IEEE Conf. on Vehicular Technology, Spring*, Birmingham, AL, May 2002, vol. 3, pp. 1200–1204.

[5] C. Prettie, D. Cheung, L. Rusch, and M. Ho, "Spatial correlation of UWB signals in a home environment," in *Proc. IEEE Conf. on Ultra Wideband Systems and Technologies*, Baltimore, MD, May 2002, pp. 65–69.

[6] A. Durantini, W. Ciccognani, and D. Cassioli, "UWB propagation measurements by pn-sequence channel sounding," in *Proc. IEEE Conf. on Communications*, Paris, France, Jun. 2004, vol. 6, pp. 3414–3418.

[7] A. Durantini and D. Cassioli, "A multi-wall path loss model for indoor UWB propagation," in *Proc. IEEE Conf. on Vehicular Technology, Spring*, Stockholm, Sweden, May 2005, vol. 1, pp. 30–34.

[8] J. Kunisch and J. Pump, "Measurement results and modeling aspects for UWB radio channel," in *IEEE Conf. on Ultra Wideband Systems and Technologies*, Baltimore, MD, May 2002, pp. 19–23.

[9] J. Keignart and N. Daniele, "Subnanosecond UWB channel sounding in frequency and temporal domain," in *Proc. IEEE Conf. on Ultra Wideband Systems and Technologies*, Baltimore, MD, May 2002, pp. 25–30.

[10] S. S. Ghassemzadeh, L. J. Greenstein, T. Sveinsson, A. Kavcic, and V. Tarokh, "UWB delay profile models for residential and commercial indoor environments," *IEEE Trans. Veh. Technol.*, vol. 54, no. 4, pp. 1235–1244, Jul. 2005.

[11] A. F. Molisch, K. Balakrishnan, D. Cassioli, C.-C. Chong, S. Emami, A. Fort, J. Karedal, J. Kunisch, H. Schantz, U. Schuster, and K. Siwiak, "A comprehensive model for ultrawideband propagation channels-," in *Proc. IEEE Conf. on Global Communications*, St. Louis, MO, Mar. 2005, vol. 6, pp. 3648–3653.

[12] W. Zhang, T. D. Abhayapala, and J. Zhang, "UWB spatial-frequency channel characterization," in *Proc. IEEE Vehicular Technology Conf., Spring*, May 2006, vol. 6, pp. 2891–2895.

[13] H. Hashemi, "The indoor radio propagation channel," *Proc. IEEE*, vol. 81, pp. 943–968, Jul. 1993.

[14] X. Li and K. Pahlavan, "Super-resolution TOA estimation with diversity for indoor geolocation," *IEEE Trans. Wireless Commun.*, vol. 3, no. 1, pp. 224–234, Jan. 2004.

[15] A. Moghaddar, Y. Ogawa, and E. K. Wolton, "Estimating the time-delay and frequency decay parameter of scattering components using a modified music algorithm," *IEEE Trans. Antennas Propag.*, vol. 42, no. 10, pp. 1412–1418, Oct. 1994.

[16] R. Carriere and R. L. Moses, "High resolution radar target modeling using a modified Prony estimator," *IEEE Trans. Antennas Propag.*, vol. 40, no. 1, pp. 13–18, Jan. 1992.

[17] R. C. Qiu and I.-T. Lu, "Multipath resolving with frequency dependence for wide-band wireless channel modeling," *IEEE Trans. Veh. Technol.*, vol. 28, no. 1, pp. 273–285, Jan. 1999.

[18] L. C. Potter, D.-M. Chiang, R. Carriere, and M. J. Gerry, "A GTD-based parametric model for radar scattering," *IEEE Trans. Antennas Propag.*, vol. 43, no. 10, pp. 1058–1067, Oct. 1995.

[19] A. Papoulis, *Probability, Random Variables, and Stochastic Processes*, 3rd ed. New York: McGraw-Hill, 1991.

[20] A. D. Whalen, *Detection of Signals in Noise*, 1st ed. Boston, MA: Academic Press, 1971.

[21] R. Luebbers, "Finite conductivity uniform GTD versus knife edge diffraction in prediction of propagation path loss," *IEEE Trans. Antennas Propag.*, vol. 32, no. 1, pp. 70–76, Jan. 1984.

[22] [Online]. Available: http://cm.bell-labs.com/cm/cs/who/bwk/wise/index.html

[23] V. Erceg, S. Fortune, J. Ling, A. Rustako, and R. Valenzuela, "Comparisons of a computer-based propagation prediction tools with experimental data collected in urban microcellular environments," *IEEE J. Sel. Areas Commun.*, vol. 15, pp. 677–684, May 1997.

[24] D. Ullmo and H. U. Baranger, "Wireless propagation in buildings: A statistical scattering approach," *IEEE Trans. Veh. Technol.*, vol. 48, no. 3, pp. 947–955, May 1999.

[25] F. A. Agelet, A. Formella, J. M. H. Rabanos, F. I. de Vincente, and F. P. Fontan, "Efficient ray-tracing acceleration techniques for radio propagation modeling," *IEEE Trans. Veh. Technol.*, vol. 49, no. 6, pp. 2089–2104, Nov. 2000.

[26] A. Muqaibel, S.-J. Bayram, A. M. Attiya, and S. M. Riad, "Ultrawideband through-the-Wall propagation," *Proc. Inst. Elect. Eng. Microw., Antennas Propag.*, vol. 152, no. 6, pp. 581–588, Dec. 2005.

[27] F. Sagnard and G. E. Zein, "In situ characterizations of building materials for propagation modeling: Frequency and time responses," *IEEE Trans. Antennas Propag.*, vol. 53, no. 10, pp. 3166–3173, Oct. 2005.

[28] A. Muqaibel, A. Safaai-Jazi, A. Bayram, and S. M. Riad, "Ultra wideband material characterization for indoor propagation," in *Proc. IEEE Antennas and Propagation Society Symp.*, Columbus, OH, Jun. 2003, vol. 4, pp. 623–626.

[29] Y. P. Zhang and Y. Hwang, "Measurements of the characteristics of indoor penetration loss," in *Proc. IEEE Vehicular Technology Conf., Spring*, Stockholm, Sweden, Jun. 1994, vol. 3, pp. 1741–1744.

[30] G. German, Q. Spencer, L. Swindlehurst, and R. Valenzuela, "Wireless indoor channel modeling: Statistical agreement of ray tracing simulations and channel sounding measurements," in *Proc. IEEE Conf. on Acoustics, Speech, and Signal Processing*, Salt Lake City, UT, May 2001, vol. 4, pp. 2501–2504.

[31] J. Kraus, *Electromagnetics*, 3rd ed. New York: McGraw-Hill, 1984.

# Integration of Yagi Antenna in LTCC Package for Differential 60-GHz Radio

M. Sun, Y. P. Zhang, K. M. Chua, L. L. Wai, D. Liu, and B. P. Gaucher

*Abstract*—A Yagi antenna implemented in a thin cavity-down ceramic ball grid array package in low temperature cofired ceramic (LTCC) technology is reported. The antenna, intended for use in highly integrated differential 60-GHz radios, has achieved a 10-dB impedance bandwidth of 2.3 GHz from 60.6 to 62.9 GHz and a peak gain of 6 dBi at 62 GHz.

*Index Terms*—60-GHz radio, antenna-in-package (AiP), low temperature cofired ceramic (LTCC).

## I. INTRODUCTION

An IEEE standards group 802.15.3c is defining specifications for 60-GHz radio to use a few Gigahertz of unlicensed spectrum to enable very high-data-rate applications, such as high-speed Internet access, streaming content downloads, and wireless data bus for cable replacement. The targeted data rate for these applications is greater than 2 Gb/s [1]. For the 60-GHz radio, in order to have mass deployment and meet consumer marketplace requirements the cost and size of any solution has to be low and compact. In fact, designs towards low-cost highly-integrated 60-GHz radio have been carried out in silicon technologies. For example, Brian, *et al.* demonstrated the first experimental 60-GHz radio transmitter and receiver chipset in a $0.13$-$\mu$m silicon-germanium (SiGe) technology [2] and Razavi a 60-GHz radio transceiver chip in a $0.13$-$\mu$m complementary metal oxide semiconductor (CMOS) technology [3]. These highly-integrated 60-GHz radios are designed with differential architectures. A differential architecture is of great advantage in current silicon technology for highly-integrated radios because the differential nature permits higher linearity, lower offset, makes it immune to power supply variations and substrate noise. Thus, exploring the design of differential antenna is essential for these radios to get rid of off-chip or lossy on-chip baluns.

Antenna designs for radio operating at 60 GHz or above are turning to antenna-on-chip (AoC) and antenna-in-package (AiP) solutions [4]–[7]. This is because the antenna form factor at 60 GHz is on the order of millimetres or less, which opens up new integration options on a chip or in a package. Zhang, *et al.* evaluated the AoC solution for 60-GHz radio on a silicon substrate and found that both inverted-F and quasi-Yagi on-chip antennas have very poor radiation efficiency about 5% due to the low resistivity and high permittivity of the silicon substrate [4]. Micromachining techniques and proton implantation process have been proposed to reduce silicon substrate loss so as to improve the AoC radiation efficiency [5], [6]. Pfeiffer, *et al.* demonstrated a complete AiP solution for 60-GHz radio in a plastic land grid array package and a folded dipole (differential) antenna suspended in